

Cluster Bulleticity

Richard Massey¹, Thomas Kitching¹ & Daisuke Nagai^{2,3}

¹*University of Edinburgh, Royal Observatory, Blackford Hill, Edinburgh EH9 3HJ, UK* rm,tdk@roe.ac.uk

²*Department of Physics, Yale University, New Haven, CT 06520, USA* daisuke.nagai@yale.edu

³*Yale Center for Astronomy & Astrophysics, New Haven, CT 06520, USA*

13 January 2011

ABSTRACT

The unique properties of dark matter are revealed during collisions between clusters of galaxies, like the bullet cluster (1E 0657-56) and baby bullet (MACSJ0025-12). These systems provide evidence for an additional, invisible mass in the separation between the distribution of their total mass, measured via gravitational lensing, and their ordinary ‘baryonic’ matter, measured via its X-ray emission. Unfortunately, the information available from these systems is limited by their rarity. Constraints on the properties of dark matter, such as its interaction cross-section, are therefore restricted by uncertainties in the individual systems’ impact velocity, impact parameter and orientation with respect to the line of sight.

Here we develop a complementary, statistical measurement in which every piece of substructure falling into every massive cluster is treated as a bullet. We define ‘bulleticity’ as the mean separation between dark matter and ordinary matter, and we measure the signal in hydrodynamical simulations. The phase space of substructure orbits also exhibits symmetries that provide an equivalent control test.

Any detection of bulleticity in real data would indicate a difference in the interaction cross-sections of baryonic and dark matter that may rule out hypotheses of non-particulate dark matter that are otherwise able to model individual systems. A subsequent measurement of bulleticity could constrain the dark matter cross-section. Even with conservative estimates, the existing HST archive should yield an independent constraint tighter than that from the bullet cluster. This technique is then trivially extendable to, and benefits enormously from larger, future surveys.

Key words: dark matter — galaxies: clusters: general — cosmology.

1 INTRODUCTION

The standard Λ CDM cosmological model includes a component of cold dark matter that amounts to 85% of the matter content of the Universe. This dark matter affects the Universe primarily through gravity, and is necessary to explain the distribution and growth of large scale structure over cosmic time. However, dark matter does not interact (or only very weakly) in the electroweak sector.

The fundamentally different properties of dark matter and baryonic matter are highlighted most dramatically in their temporary separation during collisions between galaxy cluster pairs, such as 1E 0657-56 (Clowe, Gonzalez & Markevitch 2004; Clowe et al. 2006; Bradač et al. 2006) and MACSJ0025-12 (Bradač et al. 2008). These ‘bullet clusters’ have provided astrophysical constraints on the interaction cross-section σ of hypothesised dark matter particles, and may ultimately prove the most useful laboratory in which to test for any velocity dependence of the cross section. Unfortunately, the utility of a small number of individual systems

is limited by observational uncertainties in their collision velocity, impact parameter and angle with respect to the plane of the sky (Randall et al. 2008). Current constraints are 3 orders of magnitude weaker than constraints from the shapes of haloes (Feng 2010) and, since collisions between two massive progenitors are rare (Shan, Qin & Zhao 2010), the total observable number of such systems may be inadequate to investigate a physically interesting regime of dark matter properties.

In this paper, we present a statistical method that allows every piece of substructure falling into every cluster to contribute to a global measure of dark matter-baryonic separation that we refer to as ‘bulleticity’. In this approach, every infalling mass is treated as a bullet, whose (interacting) gas is expected to collide with the intra-cluster medium (ICM) and lag behind the (non-interacting) dark matter (Powell, Kay & Babul 2009). Although offsets between baryonic gas (e.g. as seen in X-ray emission) and total mass (e.g. as seen by gravitational lensing) may not be *individually* significant, detecting a mean bulleticity across many systems would pro-

vide robust evidence for a difference between the baryonic matter and dark matter interaction cross-sections. Measurements of the *amplitude* of bulleticity could then constrain the level of the dark matter-dark matter and dark matter-baryonic cross-sections. Crucially, since bulleticity should be observable in the ongoing assembly of every massive structure throughout the Universe, our statistical technique can overcome the previous limitations of small number statistics.

This paper is organised as follows. In Section §2, we develop a simple physical model to illustrate the concept of bulleticity and explore some of its dependencies. In Section §3, we use full hydrodynamical calculations to measure the expected bulleticity signal in realistic galaxy clusters. In Section §4, we discuss the practicality of measurements from real astronomical data and use a Fisher matrix analysis to predict constraints on the interaction cross-section of dark matter using various data sets. We conclude in Section §5.

2 DYNAMICAL MODEL

2.1 Motion of test particles falling into clusters

We shall illustrate the dominant physical effects that separate components of dark and baryonic mass as they fall into a massive cluster. Throughout, we shall refer to the combined infalling system as a ‘bullet’.

Consider the rest frame of a cluster with fixed ‘singular isothermal sphere’ 3D mass distribution $\rho(r) = \rho_0(r_0/r)^2$, which has a mass interior to radius r of $M(< r) = 4\pi\rho_0 r_0^2 r$. An infalling, point-like component at position \mathbf{r} , which interacts only gravitationally, has an equation of motion

$$\frac{d^2\mathbf{r}}{dt^2} = -\frac{4\pi G\rho_0 r_0^2}{r^2}\mathbf{r}, \quad (1)$$

where t is the proper time for the cluster and r is the 3D radius.

An equivalent component that also interacts via the electroweak force experiences additional pressure support. We approximate this interaction as a buoyancy force equal to the weight of the displaced mass. For a sufficiently small bullet that the density $\rho(r)$ of the cluster is constant across it, the equation of motion is

$$\frac{d^2\mathbf{r}}{dt^2} \approx -\frac{4\pi G\rho_0 r_0^2}{r^2} \left(1 - (137\alpha)^2 \frac{\rho_0 r_0^2}{\rho_b r^2}\right) \mathbf{r}, \quad (2)$$

where α is the dimensionless coupling constant and ρ_b is the mean (total) density of the bullet, assuming that the ratio of baryons to dark matter is the same in the cluster and the bullet.

We shall use equation (1) with $\alpha = 0$ to model the dynamics of standard cold dark matter and equation (2) with $\alpha = 1/137$ to model baryonic matter. To study interacting dark matter, we can simply add a nonzero α term, which represents the mean of the dark matter-dark matter and dark matter-baryonic coupling constants, weighted by the ratio in which the two forms of matter are found in the cluster. Such particles would follow orbits between those of standard dark matter and baryons. The $(137\alpha)^2$ prefactor can be interpreted as either the fractional volume of cluster mass displaced by a solid bullet, or as the fractional cross-section seen by an interacting particle, i.e. for a geometrically thin bullet $(137\alpha)^2 \approx \sigma/\pi r_b^2$.

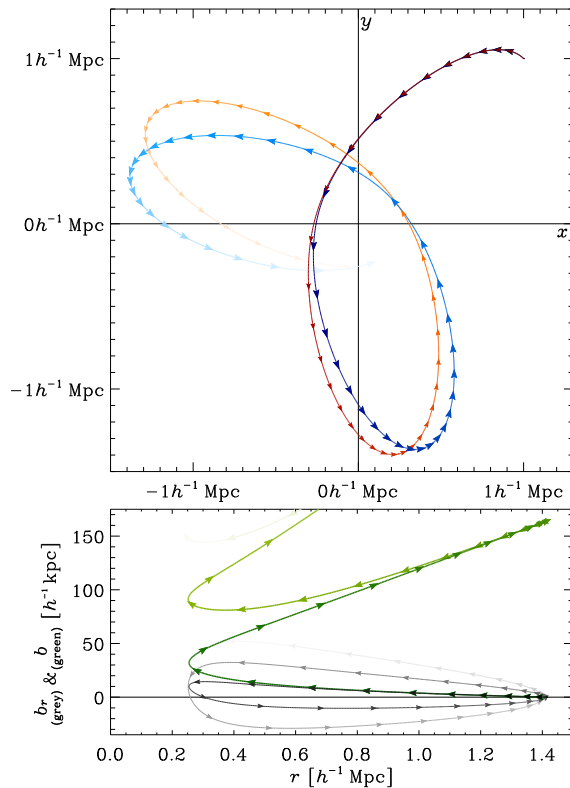


Figure 1. Orbits of test particles falling into a $10^{14} M_{\odot}$ ‘singular isothermal sphere’ cluster. In the top panel, the blue curve (large arrows) shows the trajectory of standard, non-interacting $\alpha = 0$ cold dark matter, which is governed in this simple model purely by the gravitational attraction from the central mass. The red curve (small arrows) shows the trajectory of $\alpha = 1/137$ baryonic matter, which experiences an additional buoyancy force. Arrowheads are spaced uniformly in proper time, and the paths progressively fade. The bottom panel shows the apparent bulleticity if the substructure is moving in the plane of the sky.

Note that both dark and baryonic matter also experience dynamical friction and tidal gravitational forces, but equally – so that neither of these effects should separate the two components. To keep our model simple, we therefore ignore these effects, but note that the dissipation of the bullet due to tidal and ram-pressure stripping, in conjunction with the finite crossing time of a typical cluster, means that we would only ever expect to see bullets on their first one or two passes through a cluster. Whilst the dynamical friction of a lumpy intra-cluster medium would begin to circularise the bullet’s orbit during this time, we also neglect this effect.

2.2 Definition of bulleticity

We define bulleticity \mathbf{b} as the vector from the position of the dark matter, projected onto the plane of the sky, to that of the baryons. Its magnitude is thus sensitive to the difference $\Delta\sigma$ in the total interaction cross-sections of dark matter and baryons. Were all matter to have the same interaction cross-section, this would ensure $\mathbf{b} \equiv \mathbf{0}$. Any non-zero detection will therefore indicate the presence of nonbaryonic material.

We define the location of the bullet to be the mean position (r, θ) of the dark matter and the baryons projected

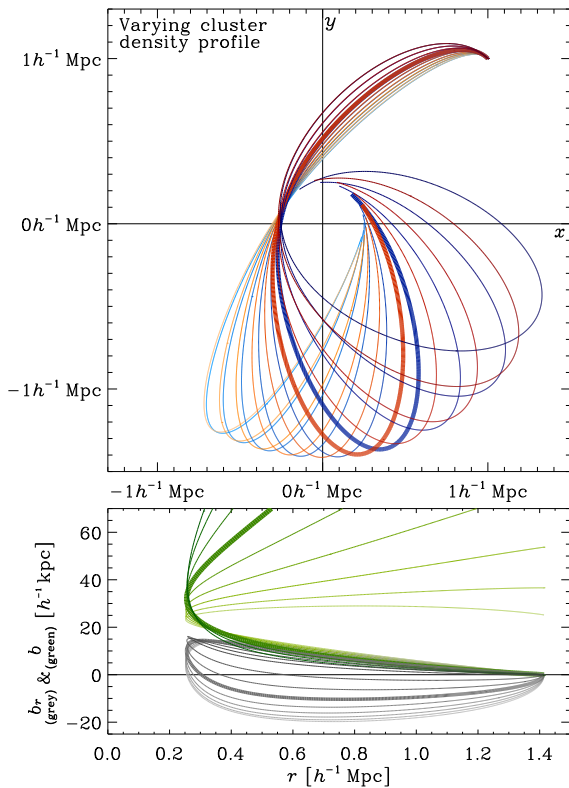


Figure 2. Varying the power law slope of the density profile $\rho \propto r^\gamma$ between $\gamma = -1$ (light) and $\gamma = -2.6$ (dark) in steps of 0.2 , for a fixed cluster mass and bullet density, while adjusting the bullet's initial velocity to also ensure a constant impact parameter. Notice that $\partial b / \partial \gamma$ is small around $\gamma = -2$ (thick line). To avoid confusion, the orbits are only traced up to the second periapsis (point of closest approach), and bulleticity to the second apoapsis.

onto the sky. In general, these need not be the same. We need to uniquely define the location of each bullet because its bulleticity can depend upon the length of time it has been within a cluster, and the path it has previously traversed. Henceforth, we shall use the symbol r to represent this 2D projected radius.

In the 1D case of a bullet that falls into a cluster potential along a radius, equations (1) and (2) both produce oscillatory motion (with the caveat of a numerical finesse at the origin to remove the point of infinite density). However, as the baryons experience extra buoyancy, they gradually lag behind the dark matter: farther from the cluster core during infall and closer to the core during egress. The absolute bulleticity $b = |\mathbf{b}|$ steadily increases.

The 2D orbit of a bullet with non-zero impact parameter but in the plane of the sky is illustrated in Figure 1. In this calculation, we assume a cluster of mass $10^{14} M_\odot$ within $0.8 h^{-1} \text{ Mpc}$ and adopt a value of $\rho_b = 10^6 M_\odot / (h^{-1} \text{ kpc})^3$ for the baryons; the resulting bulleticity is inversely proportional to this value. To show the bulleticity more clearly, the trajectory is extended to include several passes through the cluster, during each of which the separation of dark and baryonic matter visibly increases. At each point along the mean trajectory, the green line in the bottom panel shows the absolute bulleticity $b(r)$. During the first infall, the sepa-

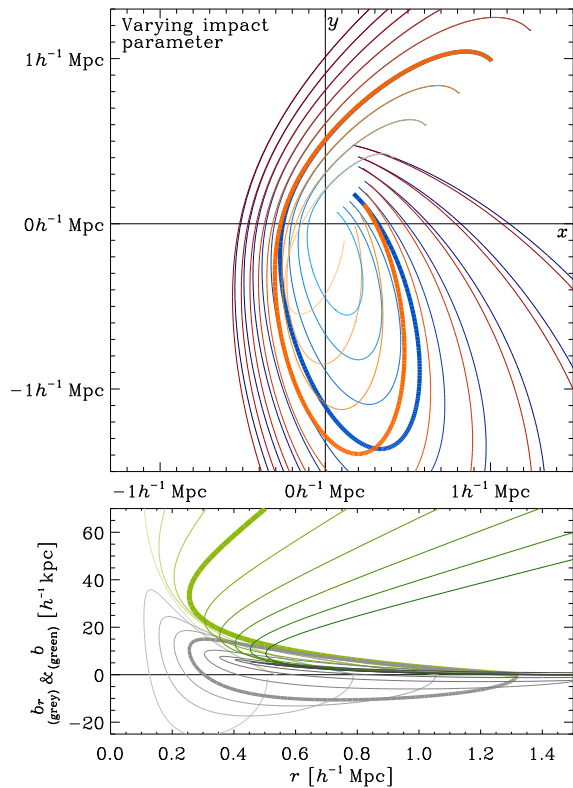


Figure 3. Changing the impact parameter from 100 to $500 h^{-1} \text{ kpc}$ in steps of $50 h^{-1} \text{ kpc}$ (while keeping the impact velocity and the cluster profile fixed). The default $250 h^{-1} \text{ kpc}$ orbit is shown as a thick line. The orbit clearly has a more dramatic influence than the cluster's density profile (Figure 2), so building a theoretical prediction for real clusters will clearly require an integration over initial phase space conditions.

ration gradually increases, with baryons lagging behind dark matter as in the 1D case. On each subsequent pass, the two components separate at large radii, as they follow different trajectories, but return to each other as they near the cluster core.

The bulleticity vector can be conveniently written in terms of components that are radial b_r and azimuthal b_t with respect to the centre of the cluster, such that

$$\mathbf{b} = b_r \hat{\mathbf{e}}_r + b_t \hat{\mathbf{e}}_t, \quad (3)$$

where $\hat{\mathbf{e}}_r$ and $\hat{\mathbf{e}}_t$ are unit vectors. This is illustrated in figure 4. While the radial and tangential bulleticity components are smaller than the absolute bulleticity $b = |\mathbf{b}|$, the crucial point is that they are signed. When averaging over all possible viewing angles or the phase space of possible bullet orbits, the mean tangential separation averages to zero (it can be easily demonstrated in this case by switching the handedness of the orbit to produce a mirror image of Figure 1). Such symmetries ensure that, for a large sample of bullets, $\langle b_t \rangle \equiv 0$. The remaining, non-zero component of radial bulleticity b_r is shown in Figure 1 as a grey line.

We thus propose two complementary bulleticity estimators. The absolute bulleticity b is positive definite, so is likely to provide the first detection of a difference in the behaviour of dark and baryonic matter at relatively large S/N. The radial bulleticity b_r has a smaller signal, but subsequent measurements from a large cluster sample will benefit from

its corresponding statistical check for systematics, b_t . This latter combination should eventually provide the method's cleanest constraints on the interaction cross-section of dark matter.

2.3 Robustness to astrophysical variation

The distribution of mass in the cluster affects the orbits of a bullet. As shown in Figure 2, dark matter precesses around a cuspy mass (converging to Keplerian orbits in the limit of a point-like central mass, with the mass at one focus of the ellipse), but has constant elliptical orbits around a cored cluster, with the centre of the mass at the centre of the ellipse. Importantly however, for a fixed impact parameter, the bulleticity of substructure on its first pass through a cluster changes by less than 5% for a wide range of cluster profiles. This lack of influence means that, to first order, uncertainty about the unknown mass distribution can be ignored, and one can freely average results from a large ensemble of clusters. It also means that bulleticity measurements are unlikely to constrain the density profile of galaxy clusters. However, other methods are expected to constrain this independently (Massey, Kitching & Richard 2010).

Conversely, varying a bullet's impact parameter does affect its subsequent bulleticity. As shown in Figure 3, baryons with a low impact parameter pass through more of the intra-cluster medium, experience greater buoyancy, and exhibit larger bulleticity after periapsis. Bullets with a low impact velocity accumulate a greater impulse from buoyancy, so also have a higher bulleticity – especially in the tangential direction, i.e. $b_t \gg b_r$. Deriving quantitative predictions about the level of bulleticity expected in real clusters will therefore require integrations over the phase space of initial conditions and subsequent orbits in a typical cosmology, as well as detailed modelling of the growth and early infall of substructure. Such analysis is beyond our simple physical model. To do this properly, we shall now switch to full hydrodynamical calculations, which also automatically include the more subtle physical effects that we have disregarded so far.

3 FULL HYDRODYNAMICAL CALCULATION

3.1 Properties of the simulations

We shall now measure the bulleticity signal in realistic, high-resolution hydrodynamical simulations of massive clusters embedded in a standard cosmological model. The model is flat, with parameters $\Omega_m = 1 - \Omega_\Lambda = 0.3$, $\Omega_b = 0.04286$, $h = 0.7$ and $\sigma_8 = 0.9$, where the Hubble constant is defined as $100 h \text{ km s}^{-1} \text{ Mpc}^{-1}$ and σ_8 is the mass variance within spheres of radius $8 h^{-1} \text{ Mpc}$. All distances are expressed in comoving coordinates.

We performed our simulations with the Adaptive Refinement Tree (ART) N -body+gasdynamics code (Kravtsov 1999; Kravtsov et al. 2002), which uses adaptive refinement in space and time, and (non-adaptive) refinement in mass (Klypin et al. 2001) to resolve high dynamic ranges. The spatial resolution in the cores of halos is $\sim 6 h^{-1} \text{ kpc}$ and the particle mass is $3\text{--}9 \times 10^8 h^{-1} M_\odot$. The formation of galaxy clusters is followed from cosmological initial conditions through later properties of the intracluster medium in-

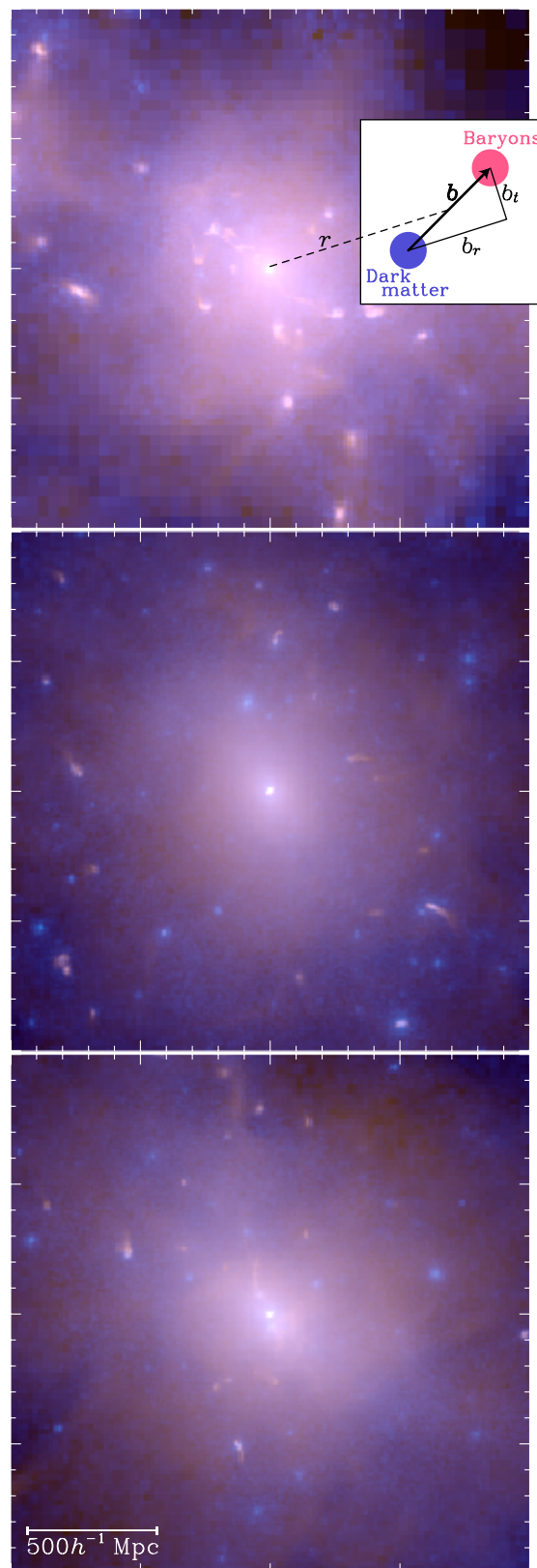


Figure 4. Full hydrodynamical simulations of massive clusters at redshift $z = 0.6$. Blue shows total projected mass (dominated by dark matter) and red shows X-ray emission from baryonic gas. The preferential trailing of gas due to pressure from the ICM, and its consequent separation from the non-interacting dark matter, is apparent in much of the infalling substructure.

Table 1. Mean properties of the simulated clusters.

	N_{cluster}	N_{bullet}	Mass M_{500} [$10^{14} M_{\odot}$]	Size r_{500} [$h^{-1} \text{ Mpc}$]
Redshift $z = 0.6$				
All	48	1142	1.2 ± 0.2	0.75 ± 0.05
Relaxed	16	303	1.6 ± 0.5	0.79 ± 0.09
Unrelaxed	32	839	1.0 ± 0.2	0.68 ± 0.04
Redshift $z = 0$				
All	48	1079	2.9 ± 0.6	0.73 ± 0.06
Relaxed	27	453	2.0 ± 0.6	0.66 ± 0.07
Unrelaxed	21	626	3.6 ± 0.9	0.79 ± 0.08

cluding gas cooling and star formation (CSF). Astrophysical processes in our simulations include metal enrichment and thermal feedback due to Type Ia and Type II supernovae, self-consistent advection of metals, metallicity-dependent radiative cooling and UV heating due to a cosmological ionising background. Potentially relevant physical processes excluded from the simulations are active galactic nuclei bubbles, magnetic fields, and cosmic rays, although these are most important in the innermost cluster regions, which we shall exclude anyway. More details about our simulations are available in Nagai et al. (2007a, b).

We realise simulated 2D observations of 16 independent clusters at two redshifts $z = 0.6$ and $z = 0$ by projecting snapshots of the dark matter density, gas density and gas temperature along three orthogonal axes. This produces 48 cluster realisations at each redshift, some of which are illustrated in Figure 4. Like the simulations by Powell, Kay & Babul (2009), ours show complex interactions of substructure. Mock *Chandra* X-ray imaging was used to visually classify each projection as either relaxed or unrelaxed (Nagai et al. 2007b). The cluster masses M_{500} span a range of about an order of magnitude centered on $10^{14} M_{\odot}$, and Table 1 lists the mean mass M_{500} , size r_{500} and number of bullets N_{bullet} in several sub-samples, where the extent of the cluster defined to be the sphere in which the mean density is 500 times the critical density of the Universe at that epoch.

3.2 Analysis of the simulations

We apply unsharp masking to maps of both the lensing mass and the baryonic gas density squared times the square root of the temperature (equivalent to the X-ray emission only if it is due to thermal bremsstrahlung, but the rest of our analysis is completely robust to this simplification). We then find the best-fit Gaussian to every local maximum via the iteration in size and position adopted by Rhodes, Réfrégier & Groth (2000). This algorithm is robust but may not be optimal in the regime of real observational noise and beam smearing. Even in our noiseless simulations, measurements near the cluster core are hindered by the steep background gradient from central emission, particularly in the X-ray signal, which pulls the best-fitting peak inward. More sophisticated algorithms might prevent this, such as simultaneous fitting of all the sources (c.f. Marshall 2006). However, we circumvent the issue by ignoring the (very few) peaks within $200 h^{-1} \text{ kpc}$ of the cluster centre. We cross-match X-ray peaks to their nearest lensing peak projected within

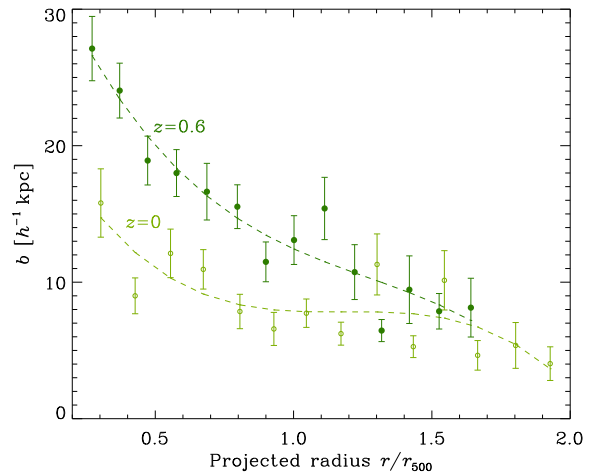


Figure 5. Measurements of absolute bulleticity from full hydrodynamical simulations. Error bars show 1σ errors. Dashed lines are best-fitting cubic polynomials to guide the eye. As expected for orbits in which only the first crossing has been completed, bulleticity increases as the infalling group falls towards the cluster centre and the gas is preferentially retarded.

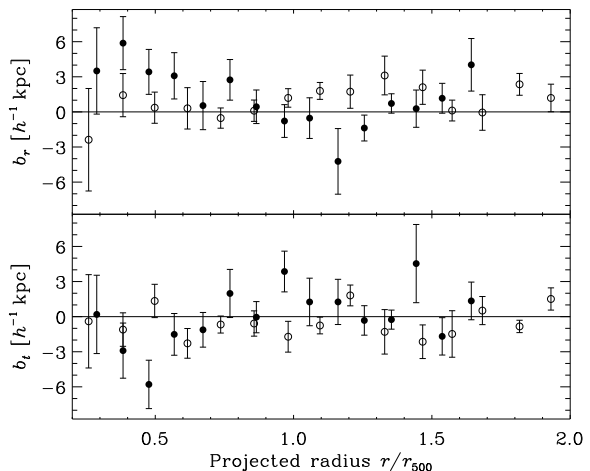


Figure 6. Measurements of radial and tangential bulleticity from full hydrodynamical simulations. These quantities are signed so, once averaged over many clusters, the values are smaller than those in Figure 5. Filled circles show data from redshift $z = 0.6$ and open circles show data from $z = 0$. The only significant detection is of radial bulleticity $b_r(r < r_{500}) = 1.7 \pm 0.7 h^{-1} \text{ kpc}$ at $z = 0.6$. The mean tangential bulleticity is consistent with zero, demonstrating its utility as a control test in this harder but potentially more discriminating measurement.

$0.5 h^{-1} \text{ Mpc}$, then apply the match the other way around and keep only uniquely defined pairs.

Figures 5 and 6 show the observed mean separation between the centres of matched X-ray and lensing peaks, projected within $0.5 h^{-1} \text{ Mpc}$ on the sky and averaged over all subpeaks. The radial and tangential components b_r and b_t can be positive or negative, so they partially cancel upon averaging, while $b \equiv \sqrt{b_r^2 + b_t^2}$ is positive definite for all bullets. As in §2, we define the centre of the bullet as the mean of the X-ray and lensing positions, and we compute the components of the bulleticity vector with respect to the direction towards the global minimum of the projected gravitational

potential. As expected from the simple model in §2, the absolute bulleticity increases towards the centre of the cluster, reaching $26 h^{-1} \text{ kpc} \approx 4''$ at $r = 0.3 r_{500}$ and $z = 0.6$. The normalisation is independent of the cluster mass (at both redshifts), within a 1σ uncertainty of $4 h^{-1} \text{ kpc}$ per order of magnitude in mass. The measurements are well fit by cubic polynomials

$$b(r) = \frac{\Delta\sigma}{\pi r_b^2} (b_0 + b_1 r + b_2 r^2 + b_3 r^3), \quad (4)$$

where the coefficients $b_i = \{38.2, -51.6, 35.0, -9.2\}$ at $z = 0.6$ and $b_i = \{24.7, -43.0, 36.4, -10.3\}$ at $z = 0$, assuming a fiducial model in which the prefactor is unity. If the polynomial order is increased, the quartic coefficients are an order of magnitude lower.

The radial and tangential bulleticity signals are an order of magnitude lower and noisier. The only statistically significant detection is that $\langle b_r \rangle = 1.7 \pm 0.7 h^{-1} \text{ kpc}$ within r_{500} at $z = 0.6$. This too appears independent of cluster mass, and all other measurements are consistent with zero. In particular, that the tangential bulleticity signal is always consistent with zero demonstrates its utility as a control test for any observational systematics.

3.3 Dependence upon redshift

The bulleticity signal decreases between the two cosmic epochs we have studied. An explanation for this, in agreement with our predictions from the simple model of §2, is that the masses of clusters are considerably lower at $z = 0.6$. With a correspondingly lower infall velocity, the baryons therefore experience a larger impulse from buoyancy. Furthermore, high redshift clusters are also generally more disturbed, have more substructures per unit mass, and have larger offsets between central dark matter and gas peaks. However, the projected angle of b on the sky *increases* for nearby clusters. Were the absolute bulleticity to decline linearly with proper time between the values measured at redshifts $z = 0.6$ and 0, the expectation of $b(0.3 r_{500})$ would rise in angular size to $\sim 10''$ at $z = 0.1$ and $\sim 16''$ at $z = 0.05$.

Clusters at low redshift will make the best targets for observation. As well as their increasing bulleticity signal, nearby clusters also provide a more optimal geometry for gravitational lensing. The common misconception to the contrary may have arisen from Hamana, Takada & Yoshida (2004), who detected peaks using a matched filter of fixed $1'$ size. Nearby clusters appear larger than this on the sky, so their fixed filter produces a diminishing signal below $z \sim 0.3$. A better matched filter reveals that the signal is larger, but merely spread thin (Kubo et al. 2007, 2009). Finally, massive, low redshift clusters should contain more substructure. That our sample includes a similar amount of substructure at all redshifts is probably a selection effect because our high redshift clusters are the most massive progenitors of present-day structures, so are growing rapidly.

3.4 Dependence upon environment

None of the bulleticity signals show a statistically significant dependence upon the cluster's apparent dynamical state. However, at redshift $z = 0.6$ (0), unrelaxed clusters yielded about 1.4 (1.8) times as many bullets per cluster as relaxed

clusters, despite having slightly lower masses at $z = 0.6$. For this measurement, unrelaxed clusters might therefore provide more profitable targets.

We also tried stacking bulleticity measurements from different clusters in terms of the bullets' absolute distance from the cluster centre, rather than as a fraction of r_{500} . Because the cluster sizes vary little within our sample, the qualitative result does not change.

In particularly crowded regions of clusters, it would be possible to mismatch pairs of dark matter and baryonic projected peaks from different substructures. However, this confusion effect will dampen the measured bulleticity and, if it is a function of cluster radius, it will be most pronounced towards the centre, where the separation is largest, and the density of bullets is highest. If the aim is purely to detect bulleticity b in order to prove the existence of dark matter, this effect will therefore only make the measurement more difficult rather than producing a spurious signal.

4 PRACTICALITY OF A REAL MEASUREMENT

So far, we have maximally exploited our computationally expensive simulations by not adding noise to our mass or X-ray maps. We shall now consider the likelihood of and practical issues that will be faced by any real measurement of bulleticity.

Baryonic substructure is frequently seen in deep *Chandra* imaging (e.g. Gastaldello et al. 2009; Randall et al. 2009). Dark matter substructure can be mapped efficiently via strong gravitational lensing or flexion (Goldberg & Bacon 2005; Bacon et al. 2006), which probes gradients in the mass distribution and is therefore more sensitive to small mass peaks along a line of sight than weak shear. Coe et al. (2010) resolved ten previously unknown subpeaks at various radii within (unrelaxed) cluster A1689 using strong lensing, and Leonard et al. (2007, 2010) resolved four using flexion. Both of these measurements were made independently of the distribution of light.

Combined X-ray and gravitational lensing observations have already revealed a separation of baryons from dark matter in two real systems undergoing major mergers. In the bullet cluster 1E 0657-56, Clowe et al. (2006) measured separations of $b = 49.3'' = 152 h^{-1} \text{ kpc}$ (main cluster) and $46.1'' = 142 h^{-1} \text{ kpc}$ (bullet). In MACS J0025.4-1222, Bradač et al. (2008) measured separations of dark matter from the central gas peak of $b = 49.3'' = 228 h^{-1} \text{ kpc}$ (SE clump) and $30.1'' = 139 h^{-1} \text{ kpc}$ (NW clump). While these measurements have small errors, it is their interpretation that remains difficult. The extreme disruption of these systems has removed any well-defined global potential minimum, so it is difficult to place the substructure at a well-defined radius r or to split the bulleticity into components b_r and b_t . Minor merger events will be more usual targets for bulleticity.

Noise in a real measurement – whether due to a finite exposure time for X-ray observations or a finite source density of lensed background galaxies – will create scatter in the measured peak positions. This will emerge as a constant minimum b signal. Indeed, this effect is tentatively seen as a value around $6 h^{-1} \text{ kpc}$ at large r in Figure 5, which coin-

cides with the resolution limit of the simulations. A resolution limit will be especially problematic in clusters at high redshift, although statistical techniques more sophisticated than an offset between peaks will inevitably help. For example, the cross-correlation between the full lensing and X-ray maps could be measured. Most importantly, measurements of the (signed) radial and tangential bulleticity from a large cluster sample will beat down noise on $\langle b_r \rangle$, and ensure that $\langle b_t \rangle \rightarrow 0$.

To predict the observable bulleticity signal, we assume that substructure positions can be resolved to $6 h^{-1}$ kpc, which is achievable with *Chandra* at $z < 0.3$. At radii where the expected bulleticity signal (4) is resolved, we assume that the observed r.m.s. error $\sigma_b(r)$ falls from the baseline of Figure 5 as $1/\sqrt{N_b}$, where N_b is the number of bullets. Once the approved Multi-Cycle Treasury programme ‘Through a lens, darkly’ (P.I. Postman) has been performed, the HST/ACS imaging archive will include ~ 50 clusters between redshifts $z = 0.1$ and 0.2 . If these clusters contain just ~ 100 substructure peaks, and even excluding measurements of those within the central $200 h^{-1}$ kpc, they should provide a detection of $b(r)$ at a signal to noise ratio of ~ 11 when integrated over scales $6 h^{-1} \text{ kpc} < r < 2r_{500}$. The Euclid survey (Massey et al. 2004; Réfrégier et al. 2010) should yield a similar detection significance for $b_r(r)$ and $b_t(r)$, even if only one substructure peak is identified in each of its $\sim 40,000$ clusters within the same redshift range.

We can estimate the tightness with which such measurements will constrain the dark matter interaction cross-section using the Fisher information matrix (Tegmark, Taylor & Heavens 1997). We again adopt the best fit models of $b(r)$ from equation (4), interpolating linearly with proper time between $z = 0.6$ and $z = 0$, and baseline observational noise $\sigma_b(r)$ around that shown in Figure 5. We assume that the bulleticity in radial bins is uncorrelated, and note that the dependence on $\Delta\sigma$ is in the mean of $b(r)$ (not the covariance). In this case, the one-parameter Fisher information is

$$\begin{aligned} F &= \sum_{\text{bullets}} \sum_r \frac{1}{\sigma_b^2(r)} \left(\frac{\partial b(r)}{\partial \Delta\sigma} \right)^2 \\ &= \sum_{\text{bullets}} \frac{1}{(\pi r_b^2)^2} \sum_r \frac{(b_0 + b_1 r + b_2 r^2 + b_3 r^3)^2}{\sigma_b^2(r)}. \end{aligned} \quad (5)$$

We have summed equally over r bins where $r > 200 h^{-1}$ kpc and $b(r) > 6 h^{-1}$ kpc, but this could be generalised to incorporate a more sophisticated weight function that raises the overall signal to noise. For the observational scenarios described above, $F(\pi r_b^2)^2 \sim 100$ for the HST archive, and $\sim 30,000$ for Euclid.

Notably, equation (5) does not depend on the fiducial value of $\Delta\sigma$. With a more comprehensive suite of hydrodynamical simulations to more accurately model the behaviour of baryonic substructure, we could therefore directly interpret constraints on $\Delta\sigma$ as those on σ . Assuming typical bullets of mass $m_b \sim 5 \times 10^{12}$ and radius $r_b \sim 10 h^{-1}$ kpc, we thus predict 68% confidence limits of

$$\left(\frac{\sigma}{m} \right) = \frac{1}{m_b \sqrt{F}} \sim \begin{cases} 1 \times 10^{-25} \text{ cm}^2/\text{GeV} & \text{for HST} \\ 6 \times 10^{-27} \text{ cm}^2/\text{GeV} & \text{for Euclid.} \end{cases} \quad (6)$$

Compare this to 68% confidence limits from the bullet cluster of $\sigma/m < 1.25 \text{ cm}^2/\text{g} = 2 \times 10^{-24} \text{ cm}^2/\text{GeV}$ or $\sigma/m <$

$0.7 \text{ cm}^2/\text{g}$ assuming that the main cluster and sub-cluster had similar mass-to-light ratios prior to the merger (Randall et al. 2008).

Even with these fairly conservative estimates, we expect a bulleticity analysis of the HST archive to produce constraints on σ similar to or tighter than the bullet cluster. Furthermore, such constraints are potentially unlimited by the uncertainty in orbital parameters for any single object. The fundamental strength of our statistical method is the trivial way in which it can then be extended to exploit larger surveys like Euclid. Bulleticity thus offers a path towards ever more discriminating measurements, even if individual extreme merger events turn out to be rare (Shan, Qin & Zhao 2010).

5 DISCUSSION

We have defined a measure of dark matter-baryonic matter separation ‘bulleticity’ that takes contributions from every detected substructure peak in every massive cluster. Any non-zero bulleticity measures the difference between the interaction cross-sections of dark and baryonic matter. This interesting new test can be understood via the intuition of a simple model, and we have also measured the expected value of the bulleticity signal using full hydrodynamical simulations of Λ CDM clusters.

A conservative estimate of currently available data and analysis techniques suggests that there should be enough information in clusters from the HST archive to detect bulleticity at a signal to noise greater than 10. With further hydrodynamical simulations to interpret the absolute level of the signal, this could yield independent constraints on the interaction cross-section of dark matter at a similar or tighter level than the bullet cluster. The real strength of this method is the way in which it can subsequently exploit large future surveys, free of biases from individual systems and in a trivially expandable way. An ambitious, all-sky survey could thus rival constraints from particle physics experiments (Feng 2010). For a targetted survey, the ideal targets would include massive, low redshift, and possibly unrelaxed clusters. Most crucially, bulleticity measurements will be obtained in a physical regime unapproachable in terrestrial laboratories, and may ultimately provide the best test for any velocity dependence of the dark matter interaction cross-section.

As a final tantalising prospect, we note that the positions of galaxies provide a third (and more easily measured) observable. Indeed, Randall et al. (2008) derived tighter constraints on the dark matter cross section by comparing the post-collision locations of dark matter and galaxies (rather than dark matter and gas). To first order, galaxies pass straight through each other unimpeded because of the separation between them, and between the stars in each galaxy. The vector from dark matter to galaxies is therefore a ‘bulleticity’ measured around a fiducial model of $\sigma = 0$, so it provides a more direct measurement of nonzero interaction cross-section. There are still potential complications to this picture. For example, Russell et al. (2010) found a group of galaxies in A2146 leading the X-ray emission as expected, but the brightest cluster galaxy lags behind it. Complex

baryonic physics can also affect observations: Cortese et al. (2007) showed that stars lead gas in galaxies that are merging into clusters, but that new star formation can also be triggered in the gas, with the new stars only gradually falling forward into the main galaxy. If such effects can be theoretically modelled, the most practical tool for this measurement is likely to be strong gravitational lensing. If the positions of peaks in a standard *LensFit* mass reconstruction (e.g. Richard et al. 2010) were allowed to float instead of being tied to the positions of galaxies, their measured offsets would be precisely this new bulleticity.

ACKNOWLEDGMENTS

The authors would like to thank Patrick Simon, Ken Rice, Phil Marshall, Cathie Clarke, Justin Read, Johan Richard and James Taylor for conversations that spurred the development of this paper. It also benefitted greatly from helpful suggestions by the anonymous referee. RM is supported by STFC Advanced Fellowship #PP/E006450/1 and ERC grant MIRG-CT-208994. TK is supported by STFC rolling grant RA0888. DN acknowledges the support of Yale University and NSF grant AST-1009811.

REFERENCES

- Bacon D., Goldberg D., Rowe B. & Taylor A., 2006, MNRAS 365, 414
- Bradač M. et al., 2006, ApJ 652, 937
- Bradač M. et al., 2008, ApJ 687, 959
- Clowe D., Gonzalez A. & Markevitch M., 2004, ApJ 604, 596
- Clowe D., Bradač M., Gonzalez A., Markevitch M., Randall S., Jones C. & Zaritsky D., 2006, ApJL 648, 109
- Coe D., Benitez N., Broadhurst T., Moustakas L. & Ford H., ApJ submitted (arXiv:1005.0398)
- Cortese L. et al., 2007, MNRAS 376, 157
- Feng J., 2010, ARA&A 48, 495
- Gastaldello F., Buote D., Temi P., Brighenti F., Mathews W. & Ettori S., 2009, ApJ, 693, 43
- Goldberg D. & Bacon D., 2005, ApJ 619, 741
- Hamana T., Takada M. & Yoshida N., 2004, MNRAS 350, 893
- Kravtsov A., 1999, PhD thesis, New Mexico State University
- Kravtsov A., Klypin A. & Hoffman Y., 2002, ApJ 571, 563
- Klypin A., Kravtsov A., Bullock J. & Primack J., 2001, ApJ 554, 903
- Kubo J., Stebbins A., Annis J., Dell’Antonio I., Lin H., Khiabani H. & Frieman J., 2007, ApJ 671, 1466
- Kubo J. et al., 2009 ApJ 702 L110
- Leonard A., Goldberg D., Haaga J. & Massey R., 2007, ApJ 666, 51
- Leonard A., King L. & Goldberg D., MNRAS submitted (arXiv:1009.1018)
- Mahdavi A., Hoekstra H., Babul A., Balam D. & Capak P., 2007, 668, 806
- Marshall P., 2006, MNRAS 372, 1289
- Massey R., et al. 2004, AJ 127, 3089
- Massey R., Kitching T. & Richard J., 2010, Rep. Prog. Phys. 73, 086901
- Nagai D., Kravtsov A. & Vikhlinin A., 2007a, ApJ 668, 1
- Nagai D., Vikhlinin A. & Kravtsov A., 2007b, ApJ 655, 98
- Powell L., Kay S. & Babul A., 2009, MNRAS 400, 705
- Randall S., Markevitch M., Clowe D., Gonzalez A. & Bradač M., 2008, ApJ 670, 1173
- Randall S., Jones C., Markevitch M., Blanton E., Nulsen P. & Forman W., 2009, ApJ 700, 1404
- Réfrégier A. et al., 2009, arXiv:1001.0061
- Rhodes J., Réfrégier A. & Groth E., 2000, ApJ 536, 79
- Richard J. et al., 2010, MNRAS 404, 325
- Russell H., Sanders J., Fabian A., Baum S., Donahue M., Edge A., McNamara B. & O’Dea C., 2010, MNRAS 406, 1721
- Shan H., Qin B. & Zhao H., MNRAS in press (arXiv:1006.3484)
- Tegmark M., Taylor A. & Heavens A., 1997, ApJ 480, 22

This paper has been typeset from a T_EX/ L^AT_EX file prepared by the author.